Journal of Alloys and Compounds 948 (2023) 169713

Contents lists available at ScienceDirect

Journal of Alloys and Compounds

journal homepage: www.elsevier.com/locate/jalcom

Review

# Lanthanum modified $Fe_3N$/carbon foam as highly efficient electrode for zinc-air batteries

Minghui Wang [a], Shan Ji [b,*], Hui Wang [a], Xuyun Wang [a], Vladimir Linkov [c], Xianguo Ma [d], Rongfang Wang [a,*]

[a] State Key Laboratory Base for Eco-Chemical Engineering, College of Chemical Engineering, Qingdao University of Science and Technology, Qingdao 266042, China
[b] College of Biological, Chemical Science and Engineering, Jiaxing University, Jiaxing 314001, China
[c] South African Institute for Advanced Materials Chemistry, University of the Western Cape, Cape Town 7535, South Africa
[d] School of Chemical Engineering, Guizhou Institute of Technology, Guiyang 550003, China

ARTICLE INFO

*Article history:*
Received 13 January 2023
Received in revised form 7 March 2023
Accepted 15 March 2023
Available online 17 March 2023

*Keywords:*
Fe, N co-doped carbon
La modification
OER
ORR
Zinc-air battery

ABSTRACT

Efficient electrocatalysts for the oxygen reduction reaction (ORR) and the oxygen evolution reaction (OER) are of great importance for large-scale application of rechargeable zinc-air batteries. Iron-nitrogen-carbon materials are known for their excellent ORR catalytic activity, but it is their low OER performance that is responsible for poor charging operation causing slow market adoption of these energy storage devices. Herein, lanthanum (La) is applied to enhance OER electrocatalytic properties of iron-nitrogen-carbon materials used as zinc-air battery electrodes. According to X-ray diffractometry, the presence of La alters the electronic structure of surrounding N and Fe elements, resulting in more negative N and positive Fe ions to appear on the surface and form $Fe_3N$ active species. Electrochemical analysis demonstrated enhanced bifunctional electrocatalytic performance of La-modified $Fe_3N$ carbon foam (La-$Fe_{0.1:1}$/NFC) which total overpotential was among the lowest of previously reported metal-nitrogen-carbon materials. La-$Fe_{0.1:1}$/NFC exhibited high power density and charge-discharge cycling stability in a real zinc-air battery cell.



**Contents**



## 1. Introduction

Increasingly serious global energy crisis and environmental pollution draw research attention towards developing green sustainable energy sources as alternatives to conventional fossil fuels [1–3]. The use of appropriate energy storage technologies is the key to large

* Corresponding authors.
*E-mail addresses:* wangh@qust.edu.cn (M. Wang), jishan@zjxu.edu.cn (S. Ji), wangxy@qust.edu.cn (X. Wang), vlinkov@uwc.ac.za (V. Linkov), maxianguo@git.edu.cn (X. Ma), rfwang@qust.edu.cn (R. Wang).

https://doi.org/10.1016/j.jallcom.2023.169713
0925-8388/

scale application of solar and wind energy, due to its discontinuous nature. Among currently available energy storage devices, zinc-air batteries (ZAB) have great potential due to their high energy density, safety, and reliability [4]. Electricity storage and release in these batteries occurs through redox reactions between positive and negative electrodes, namely the oxygen reduction reaction (ORR) and the oxygen evolution reaction (OER). However, ORR and OER are kinetically sluggish and involve multi-electron processes, resulting in high overpotentials, which can be overcome by efficient electrocatalysts [5,6]. Currently available PGM-based Pt/C and $RuO_2$/$IrO_2$ commercial catalysts are not capable in simultaneous acceleration of both ORR and OER, are costly and scarce, which significantly restricts their large-scale energy storage applications [7–9]. At present, transition metal (TM) based materials are becoming strong alternatives to PGM based OER and ORR electrocatalysts used in zinc-air batteries [10–13]. However, they have low catalytic surface site density and are prone to active site aggregation, which is overcome by the use of highly porous carbon materials with large specific surface areas as catalyst supports [14–16]. It was found that heteroatom (Fe and N) doped carbons possess more catalytically active sites resulting in faster reaction kinetics [17,18]. Fe and N co-doping generates additional Fe-$N_x$ active species and improves nitrogen fixation and graphitization of carbon materials [19]. Noteworthy, the carbons containing iron nitride demonstrated ORR catalytic performance similar to that of the state-of-the-art Pt-based catalyst [11]. While many studies were focused on developing porous carbons containing iron nitride species to replace PGM-based ORR and OER catalysts, most of them reported complex procedures and expensive precursors, such as metal organic frameworks [20] and iron phthalocyanine [21]], significantly impeding possible practical applications of resulting materials. Moreover, most of described Fe-N-C catalysts were successfully used to catalyze ORR but exhibited poor OER activity, which makes them unsuitable as air cathodes in zinc-air batteries. Low-cost high performance bi-functional Fe-N-C catalysts suitable for this important application are still to be developed.

Introduction of surface dopants into Fe-N-C catalysts is an effective way to further enhance their ORR and OER performance [22–24] by altering electronic structures of adjacent atoms which improves reaction kinetics [25,26]. The rare earth element lanthanum (La) has been shown to improve materials' catalytic properties due to its unique electronic structure and a stable valence state [27]. The difference in electronegativity between La and host carbon materials allows La atoms to provide additional electrons to adjacent C atoms, enhancing conductivity of the catalyst [28–30]. In addition, La can also tune surface charge distribution by forming oxygen vacancies and induce strong electronic interactions with transition metal atoms, which improves electrocatalytic activity [31]. In particular, Sun et al. [32] used La ions to modify the surface structure of $IrO_2$ to enhance its OER activity. Furthermore, together with OER activation, La element can also be used to accelerate the ORR, like in the case of recently reported highly active and durable La-doped Pt nano-sized catalyst [33]. Therefore, it could be expected that the presence of La can simultaneously improve OER and ORR performance of a Fe-N-C electrocatalytic material.

In this study, a molten salt method was adopted to introduce La into the Fe and N co-doped carbon foam to produce bi-functional ORR and OER electrocatalysts for zinc-air batteries. The 4f outer orbital of La atom allows for easy partial delocalization of electrons and their combination with those of other atoms, improving electrocatalytic properties of novel materials [22]. The study demonstrated that La can effectively adjust electronic structures of N and Fe surface atoms resulting in the formation of highly dispersed $Fe_3N$ active species. The presence of La significantly improved Fe-N-C structure and the optimized bi-functional catalyst exhibited excellent ORR/OER activity and long-term stability in a rechargeable zinc-air battery cell.

## 2. Experimental section

### 2.1. Preparation of La-$Fe_{0.1:1}$/NFC

0.202 g of $Fe(NO_3)_3 \cdot 9\ H_2O$ was dissolved in 50 mL of deionized water, and 1.62 g of $La(NO_3)_2 \cdot 6\ H_2O$ was dissolved in 50 mL of deionized water. 1 g of peptone, 3 mL (0.03 mmol) of $Fe(NO_3)_3$ and 150 μL (0.003 mmol) of $La(NO_3)_2$ solutions were mixed with 15 mL of deionized water, followed by freeze drying for 48 h. The product was mixed with 10 g of NaCl and ball-milled at 550 rpm for 3 h. The resulting powder was transferred into a furnace and heated up to 900 ℃ with a heating ramp of 2.5 ℃/min under the nitrogen atmosphere. After heating at 900 ℃ for 1 h, the sample was cooled to room temperature and labeled as La-$Fe_{0.1:1}$/NFC.

The samples with various ratio of Fe/La (0.03/0.001, and 0.03/0.005) were also prepared under identical otherwise conditions, and labeled as La-$Fe_{0.033:1}$/NFC and La-$Fe_{0.17:1}$/NFC respectively.

### 2.2. Physical characterization

Crystalline structure of the materials was studied by X-ray electron diffraction (XRD) using Cu-K α radiation, λ = 0.15418 nm, 5° $min^{-1}$, 5°– 90°. Their morphology and porous structure were observed by scanning electron microscopy (SEM) (Carl Zeiss Ultra Plus electron microscope) and transmission electron microscopy (TEM) (JEM-2000 FX microscope). Thermogravimetric analysis (TGA) was carried out on STA8000 Frontier SQ8 thermal analyzer, and the test temperature was as high as 800 ℃ in $O_2$ atmosphere. Nitrogen adsorption-desorption isotherms and BET specific surface areas were obtained using automatic specific surface area and porosity analyzer (Quantachrome, Autosorb-iQ). Chemical states of surface elements were determined by X-ray photoelectron spectroscopy (XPS) (VG Escalab 210 spectrometer).

### 2.3. Electrochemical investigation

Electrocatalytic properties of the materials were studied in a three-electrode cell connected to a CHI-760E electrochemical workstation. The working electrode was prepared as follows: 5 mg of the catalyst was dispersed in 1 mL of Nafion / ethanol solution (0.25 wt%) by ultrasonic mixing over 30 min 8 μL of the ink containing 40 mg of the catalyst was dropped onto the surface of a polished glass-carbon rotating disc electrode and air-dried. ORR was examined in 0.1 M KOH solution with Ag/AgCl/ saturated KCl electrode and platinum wire as a reference and a counter electrode, respectively. All potentials obtained in the study were converted into standard reversible hydrogen electrode potentials (RHE) using the following equation: $E_{RHE} = E_{Ag/AgCl} + 0.059\ PH + 0.197$ V. OER was probed in a three-electrode cell using 1.0 M KOH solution as an electrolyte. The working electrode was prepared by depositing 3 mg of the catalyst on nickel foam. Carbon rod was used as a counter electrode and Hg/HgO electrode as a reference. The obtained potentials were also converted into reversible hydrogen electrode potentials by the formula: $E_{RHE} = E_{Hg/HgO} + 0.059\ PH + 0.098$ V.

A zinc-air cell was assembled using the prepared material as a cathode catalyst, zinc foil as an anode and a mixture of 6 M KOH and 0.2 M $Zn(CH_3OO)_2$ as an electrolyte. The cathode was prepared as follows: 4 mg of the catalyst, 3 μL of PTFE and 4 mg of conductive carbon black were added to 350 μL of isopropanol and stirred to obtain uniform slurry. The slurry was dried at 40 ℃ and then rolled into thin slices; a slice was pressed onto the Ni foam under a pressure of 20 MPa.

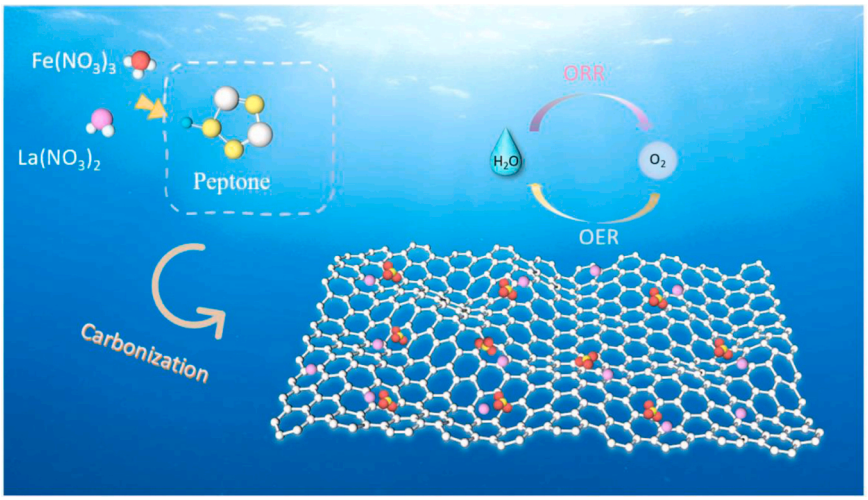


**Scheme 1.** Schematic illustration of La-$Fe_{0.1:1}$/NFC synthesis process.

## 3. Results and discussion

The preparation procedure of La-modified $Fe_3N$/carbon foam is illustrated in Scheme 1. In this study, peptone was chosen as a carbon and nitrogen source to prepare N-doped carbon. Peptone, inorganic metal salts ($Fe(NO_3)_3$, $La(NO_3)_2$) and the salt template (NaCl) were thoroughly mixed and pyrolyzed at a high temperature to form the porous carbon structure. Upon pyrolysis, NaCl melted to form nanodroplets and penetrated into the carbon precursor. The resulting carbon material attained rich porous structure, capable of facilitating charge transfer in an electrolyte and promoting the dispersion of metal species. During pyrolysis, Fe ions are easily reduced to Fe particles by the newly formed carbon material, while La element promotes the formation of $Fe_3N$ species on the surface of porous carbon; this process can be described as a one-pot molten salt method to prepare the La-modified $Fe_3N$/carbon foam. Compared with other hard templates previously used to prepare porous carbon materials, NaCl is cheap and can be removed without any complex and expensive treatments [11,34].

The crystalline structure of La-$Fe_{0.1:1}$/NFC sample was investigated by XRD as shown in Fig. 1a and S1 where diffraction peaks at 24.9° and 50.4° correspond to (002) and (102) planes of graphitic carbon, respectively (PDF#41–1487) [35]. Compared to diffraction peaks of (002) plane of Fe/NFC and La/NFC samples, the peak of La-$Fe_{0.1:1}$/NFC sample became sharper and shifted to the right, indicating higher carbon graphitization resulting from La doping. The presence of the diffraction peak of La (PDF#51–1165) in the XRD pattern of La/NFC sample (Fig. S1a), but not in that of La-$Fe_{0.1:1}$/NFC sample, is indicative of highly dispersed La nanoparticles (Fig. 1a). Compared to Fe/NFC sample (Fig. S1b), the diffraction peaks of $Fe_3N$ (PDF#49–1662) were observed in the XRD pattern of La-$Fe_{0.1:1}$/NFC (Fig. 1a), suggesting that the La doping changes the outer electronic structure of N and promotes the formation of $Fe_3N$ species.

SEM images of Fe/NFC, La/NFC and La-$Fe_{0.1:1}$/NFC samples shown in Fig. 1b and S2a, d demonstrate that a three-dimensional (3D) porous carbon network with an open structure was formed with the help of NaCl molten-salt medium at a high temperature. The absence of particles in Fig. 1c and S2 indicates the important role that the molten salt medium plays in the formation of the uniform porous carbon structure. Metal particles with diameters of less than 1 nm were observed in TEM images of La/NFC (Fig. S2b-c), congruent with the La phase structure detected in the XRD pattern of La/NFC sample. $Fe_3N$ nanoparticles of about 0.5 nm can be observed in the TEM image of La-$Fe_{0.1:1}$/NFC (Fig. 1d-e), which basically accords with the particle size distribution in Fig. 1c. TGA curves (Fig. 1f) shows two major weight losses, corresponding to water evaporation at 150 ℃ and carbon decomposition at 430 ℃, and the residual weight represents the metal mass load. TGA analysis shows that the metal loading in La-$Fe_{0.1:1}$/NFC sample is ca 0.10.65 wt%. Low metal loading can increase the high temperature sintering resistance of metal nanoclusters, and avoids the loss of ORR/OER active area of particle clusters [36]. Uniform dispersion of Fe and La in La-$Fe_{0.1:1}$/NFC sample is evident from the elemental mapping shown in Fig. 1g-i. However, the absence of Fe and La distribution overlap indicates the separation between the species containing these elements.

Specific surface area and pore size distribution of as-prepared samples were measured using $N_2$ adsorption/desorption isotherms as shown in Fig. 2 and S3. According to the IUPAC classification, all isotherms were of type II with the $N_2$ uptake at relatively low pressures and hysteresis loops at relatively high pressures. Clear nitrogen uptake visible in low pressure regions of Fig. 2a indicates the presence of micropores in La-$Fe_{0.1:1}$/NFC sample. Calculated BET surface areas of Fe/NFC, La/NFC and La-$Fe_{0.1:1}$/NFC samples were 785, 763 and 696 $m^2\ g^{-1}$, respectively, with more mesopores present in La-$Fe_{0.1:1}$/NFC than in Fe/NFC and La/NFC samples (Table S1). Abundant mesopores in La-$Fe_{0.1:1}$/NFC sample provide more active surface sites [37,38] and are beneficial for mass transfer during electrocatalytic processes [11,39].

Chemical states and composition of Fe/NFC, La/NFC and La-$Fe_{0.1:1}$/NFC samples were determined by X-ray photoelectron spectroscopy (XPS) and C, O, N, Fe and La contents are listed in Fig. S4 and Table S2. N 1 s spectra of Fe/NFC, La/NFC and La-$Fe_{0.1:1}$/NFC samples were fitted into five peaks (Fig. 3a), namely pyridine-N (398 eV), metal-N (398.7 eV), pyrrole-N (399.7 eV), graphite-N (400.8 eV) and oxide-N (405 eV) [6,40,41]. Pyridine-N (398 eV) and metal-N (398.7 eV) species, which are usually considered active ORR sites, were more prevalent in La-$Fe_{0.1:1}$/NFC sample than in other two samples [42,43]. It was previously reported that partial conversion of pyridine-N and pyrrole-N into M-N species after the coupling with metal atoms enhanced both ORR and OER electrocatalytic properties [44]. The abundance of pyridine-N and M-N species in La-$Fe_{0.1:1}$/NFC sample indicates that the La doping could promote the combination of Fe and N elements, in agreement with the high N content (5 %) presented in Table S2. As shown in Fig. 3b, Fe 2p spectra were fitted into $2p_{3/2}$ (710.4 eV, 711.7 eV), $2p_{1/2}$ (723.2 eV, 724.6 eV) and satellite (716.7 eV) peaks [45]. $Fe^{3+}$ peaks at 711.7 eV and 724.6 eV represent Fe-N bonds and $Fe^{2+}$ peaks at 710.4 eV and 723.2 eV are due to air-oxidized iron species. No obvious signals of La were detected in the high-resolution XPS spectrum of La-$Fe_{0.1:1}$/NFC (Fig. 3c), indicative of its low content and high dispersion inside the carbon matrix. The

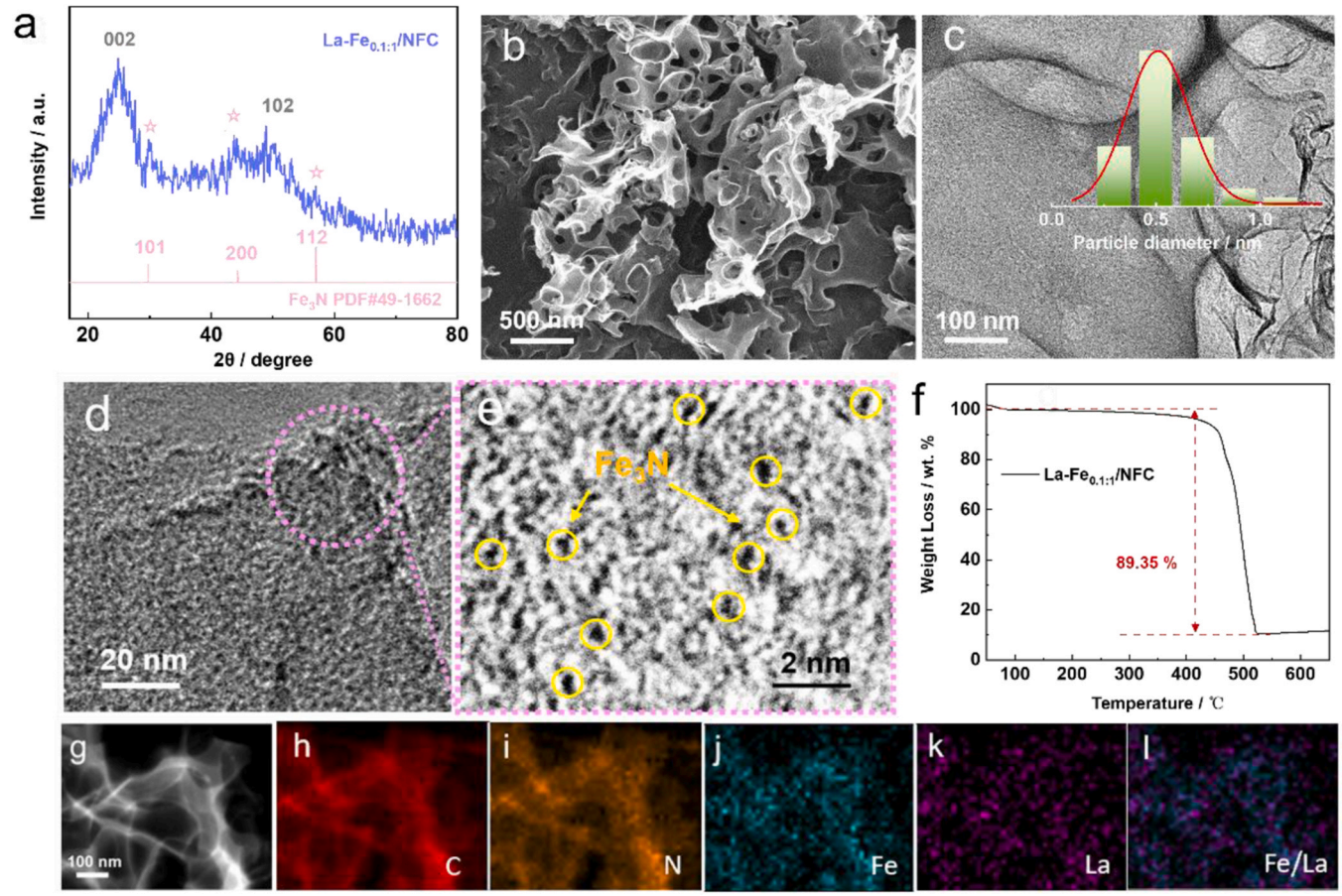


**Fig. 1.** (a) XRD pattern; (b) SEM image; (c, d) TEM images; (e) HTEM image; (f) TGA analysis; (g) STEM image; (h-j) corresponding EDS element mapping of La-$Fe_{0.1:1}$/NFC sample.

high-resolution C 1 s spectrum in Fig. 3d was deconvoluted into five peaks, i.e. C-C, C-OH, C-N, C═O and COOH [46]. The content of C-N in La-$Fe_{0.1:1}$/NFC was 11.4%, higher than those in other two samples, implying that positively charged C ions have immobilized more negatively charged N ions, which is beneficial for the promotion of intermediates adsorption and electron transfer [47,48].

Electrocatalytic activity of newly prepared materials was studied in a three-electrode cell using 0.1 M KOH as an electrolyte. Initially, the effect of La content on the ORR performance was established as shown in Fig. S5, where La-$Fe_{0.1:1}$/NFC sample has the highest onset and half-wave potentials corresponding to superior electrocatalytic activity. Since electrocatalytic reactions are surface bound, a larger electrochemical active surface area (EASA) usually represents a higher electrocatalytic activity, and is directly proportional to electrochemical double layer capacitance (EDLC). The highest EDLC of La-$Fe_{0.1:1}$/NFC sample indicates it largest EASA, which accommodates more catalytic sites (Fig. S6a).

ORR LSV responses of the samples at an electrode rotation rate of 1600 rpm are presented in Fig. 4a where La-$Fe_{0.1:1}$/NFC sample exhibits the highest onset potential (0.99 V) and half-wave potential

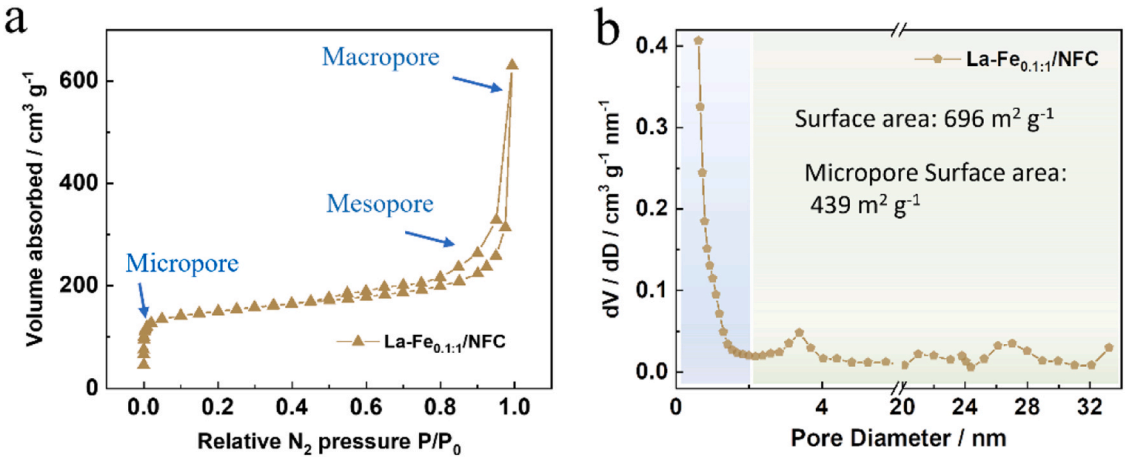


**Fig. 2.** (a) $N_2$ adsorption-desorption isotherm; (b) pore size distribution of La-$Fe_{0.1:1}$/NFC sample.

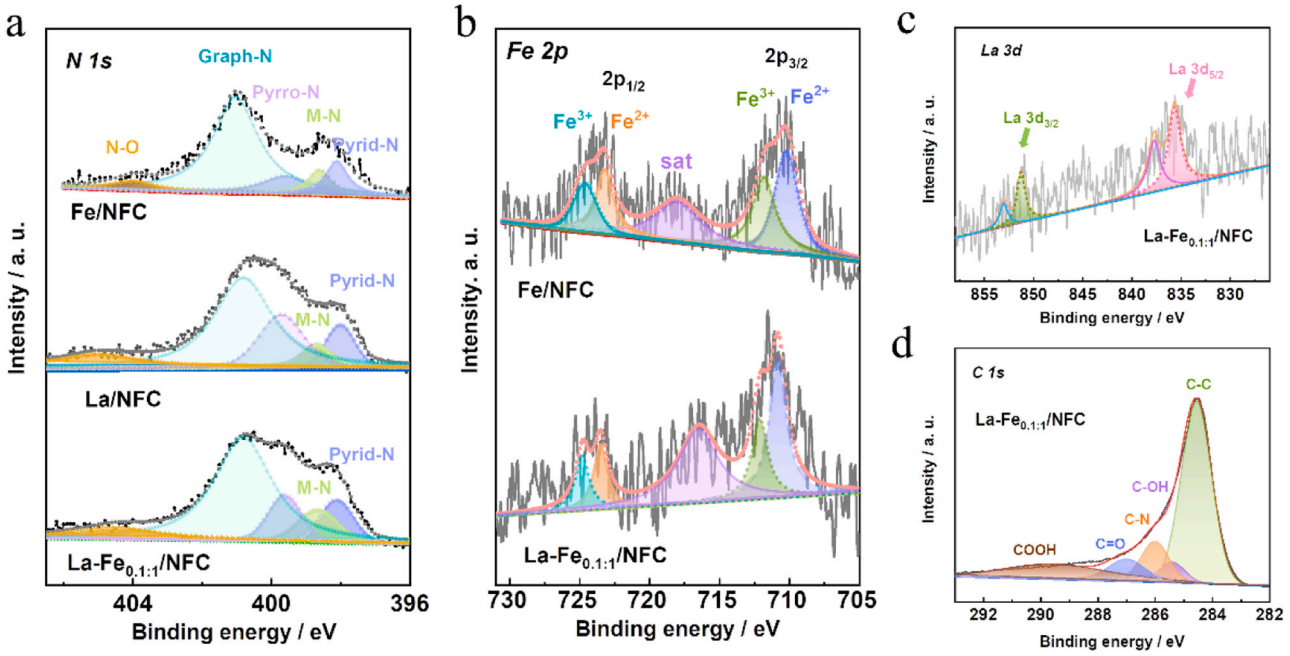


**Fig. 3.** XPS spectra of (a) N 1s; (b) Fe 2p; (c) La 3d; (d) C 1s of Fe/NFC, La/NFC and La-$Fe_{0.1:1}$/NFC samples.

(0.88 V) of ORR, even higher than corresponding values of the commercial Pt/C catalyst (Fig. 4b). Furthermore, La-$Fe_{0.1:1}$/NFC sample has the lowest among all samples Tafel slope of 55.3 mV $dec^{-1}$ (Fig. S6b), indicative of the fastest ORR kinetics. La-$Fe_{0.1:1}$/NFC reached the reaction equilibrium at 0.8 V at a current density of 5.9 mA $cm^{-2}$, demonstrating high diffusion rate and rapid adsorption/desorption of surface $O_2$. LSV curves recorded at different rotation rates were used to calculate the ORR electron transfer number according to the Koutechky-Levich (K-L) equation (Fig. 4c). At 3.8, the electron transfer number of La-$Fe_{0.1:1}$/NFC sample at 0.45–0.60 V was close to that of commercial Pt/C catalyst (Fig. S6c-d), representing a highly efficient four-electron process. After 6000 continuous CV cycles, the half-wave potential of La-$Fe_{0.1:1}$/NFC sample shifted negatively by only 21 mV, lower than that of Pt/C catalyst (Fig. S6e-f), indicating higher ORR stability of the new electrocatalyst.

The OER activity of La-$Fe_{0.1:1}$/NFC sample was also evaluated in a three-electrode cell containing 1.0 M KOH as an electrolyte. According to Figs. S7, 4d-e and S8a, La-$Fe_{0.1:1}$/NFC sample exhibited superior OER performance to those of NFC, Fe/NFC, La/NFC and $RuO_2$

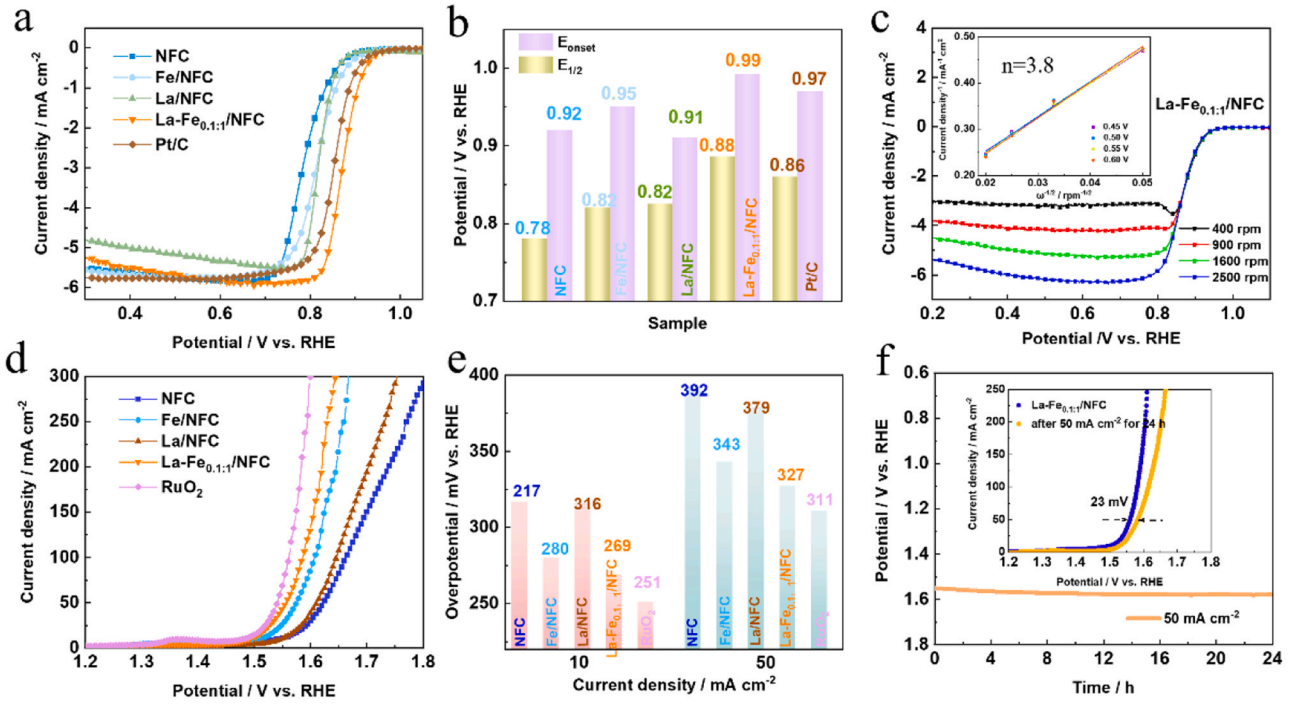


**Fig. 4.** (a) LSV curves; (b) onset ($E_{onset}$) and half-wave ($E_{1/2}$) potentials of NFC, Fe/NFC, La/NFC, La-$Fe_{0.1:1}$/NFC and Pt/C samples; (c) polarization curves of La-$Fe_{0.1:1}$/NFC sample at different rotation rates and corresponding K-L plot of ORR. (d) LSV curves; (e) overpotentials at 10 and 50 mA $cm^{-2}$; (f) 24 h chronoamperometric (CP) curve of La-$Fe_{0.1:1}$/NFC sample at 50 mA $cm^{-2}$ (inset: initial and 24 h LSV curves at 50 mA $cm^{-2}$) of OER.

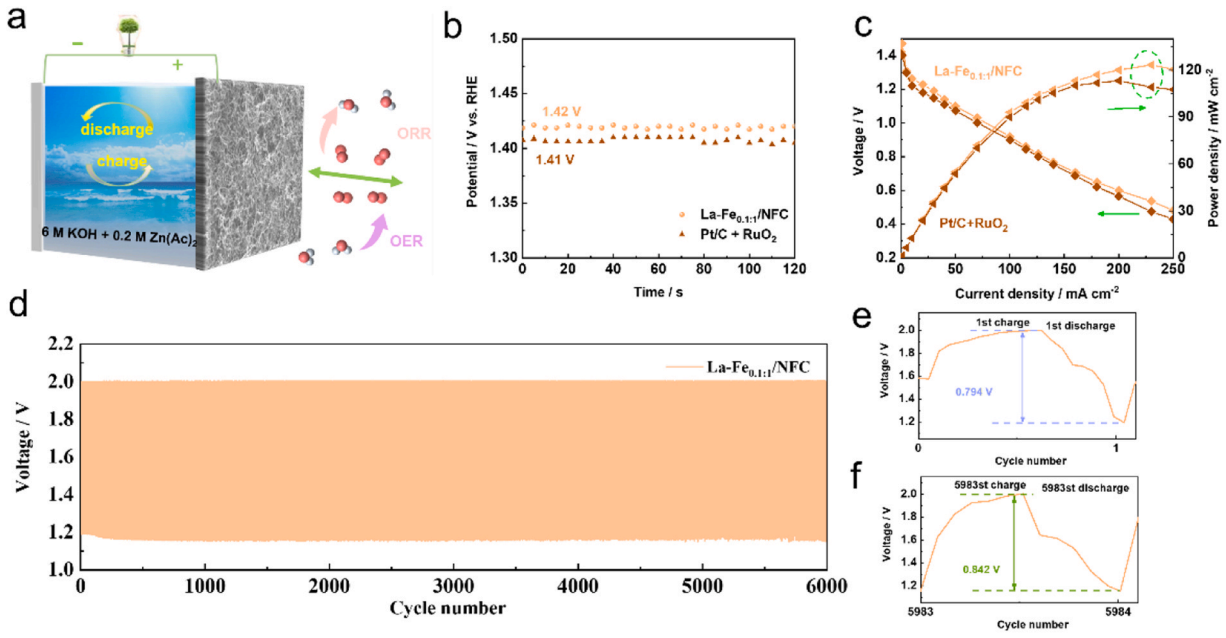


**Fig. 5.** (a) Schematic illustration of zinc-air cell; (b) open circuit voltages; (c) polarization and power density curves of La-$Fe_{0.1:1}$/NFC and Pt/C+$RuO_2$ containing cell; (d) galvanostatic charge/discharge cycling curves at 20 mA $cm^{-2}$; comparison of energy efficiency at (e) 1st and (f) 5983th cycles of La-$Fe_{0.1:1}$/NFC containing zinc-air cell.

samples, manifested by its lower overpotentials and Tafel slopes at current densities of 10 and 50 mA $cm^{-2}$. According to Nyquist plots shown in Fig. S8b, where the arc radius of La-$Fe_{0.1:1}$/NFC sample is smaller than those of other samples, this electrocatalyst has low charge transfer resistance, a crucial feature of an active electrocatalyst [49]. The relationship between ECSA and electrochemical double-layer capacitance ($C_{dl}$) allows to calculate the former using $C_{dl}$ values derived from CV scans obtained in the non-Faradaic reaction region (Fig. S9) [12]. At 30.7 mF $cm^{-2}$, $C_{dl}$ of La-$Fe_{0.1:1}$/NFC sample was significantly higher than those of other samples (Fig. S8c), pointing to more active surface sites in this new material.

Electrocatalyst stability under OER conditions was evaluated by chronoamperometry as shown in Fig. 4f, where the overpotential of La-$Fe_{0.1:1}$/NFC sample increased by only 23 mV after 24 h operation at 50 mA $cm^{-2}$, demonstrating corrosion resistance superior to that of commercial $RuO_2$ catalyst (Fig. S8d). Since the morphology, structure and composition of the catalyst are closely related to the ORR/OER performance, the SEM images of Fig. S10 and XRD spectra of Fig. S11 show that the La-$Fe_{0.1:1}$/NFC has a good structural stability during long-time cycle test.

ORR/OER bi-functional activity of electrocatalysts is represented by the ΔE value ($\triangle E = E_{j=10\ mA\ cm^{-2}} - E_{1/2}$), which, at 0.62 V, was lower for La-$Fe_{0.1:1}$/NFC sample than those for most of similar materials reported in the literature (Fig. S12 and Table S3). Excellent bi-functional electrocatalytic performance of La-$Fe_{0.1:1}$/NFC sample can be attributed to its large specific surface area and a porous structure with plenty of $Fe_3N$ active surface sites.

OER and ORR performance of La-$Fe_{0.1:1}$/NFC was studied under the real world conditions of a fully functional zinc-air cell, schematically illustrated in Fig. 5a, which was benchmarked against the similar cell containing Pt/C+$RuO_2$ as an air electrode. According to Fig. 5b, the La-$Fe_{0.1:1}$/NFC cell has an open voltage of 1.42 V, higher than that of the Pt/C+$RuO_2$ cell. The polarization and power density curves shown in Fig. 5c demonstrate that the La-$Fe_{0.1:1}$/NFC cell's power density of 121 mW $cm^{-2}$ at 250 mA $cm^{-2}$ was superior to 115 mW $cm^{-2}$ exhibited by the cell assembled with Pt/C+$RuO_2$.

According to the rate performance results shown in Fig. S13a, the voltage of the La-$Fe_{0.1:1}$/NFC cell was higher than that of the Pt/C+$RuO_2$ cell across the whole tested current range, possibly due to faster ORR kinetics of La-$Fe_{0.1:1}$/NFC. When the current density returned to 1 mA $cm^{-2}$, the voltages of both cells resumed their original values, further confirming good rate performance. According to charge/discharge curves of both cells plotted in Fig. S13b, the La-$Fe_{0.1:1}$/NFC cell has a higher discharge voltage platform accompanied by a lower potential in the tested current range, possibly due to abundant active sites on the electrocatalyst surface, which facilitate charge and electron transfer during both OER and ORR processes [50].

Long term stability of La-$Fe_{0.1:1}$/NFC in the real world zinc-air cell was studied by 6000 continuous cycles at 20 mA $cm^{-2}$, as shown in Fig. 5d. After 5983 cycles, an initial potential charge/discharge gap of 0.794 V (Fig. 5e) increased by only 0.05 V (Fig. 5f), indicating excellent stability of La-$Fe_{0.1:1}$/NFC in a zinc-air cell. The discharge stability of the La-$Fe_{0.1:1}$/NFC air cathode was evaluated during prolonged cell operation at 10 mA $cm^{-2}$, which required six zinc foil refills, achieving 250 h of total discharge time (Fig. S13c). This remarkable cell stability resulted from strong anchoring of metallic active sites on its electrode's carbon surface, which effectively prevented their aggregation.

## 4. Conclusion

La modified Fe and N-doped carbon foam with highly dispersed $Fe_3N$ active surface sites was successfully synthesized via a molten salt method, and its structure was determined using XRD, TEM, and XPS. The presence of La adjusts electronic structure of surrounding C and N atoms, which manifests itself by enhanced graphitization and increased nitrogen content, both beneficial to charge transfer during electrochemical processes. The La doping promotes more N ions to combine with Fe ions to form high-density well dispersed $Fe_3N$ active sites on the surface of carbon foam, thereby improving its electrocatalytic performance. In KOH electrolyte, the newly prepared La-$Fe_{0.1:1}$/NFC material exhibited ORR and OER electrocatalytic activity higher than those of commercial Pt/C and $RuO_2$. When used in a real zinc-air cell, La-$Fe_{0.1:1}$/NFC demonstrated superior charge/discharge stability, which makes it a promising air cathode candidate for practical battery applications.

## CRediT authorship contribution statement

**Minghui Wang**: Experiment design, Experimental operation, Date analysis, Writing original draft. **Shan Ji**: Writing–review & editing. **Hui Wang**: Guide experimental design, Modify the draft. **Xuyun Wang**: Visualization. **Vladimir Linkov**: Visualization, Writing– review. **Xianguo Ma:** Visualization. **Rongfang Wang**: Conceptualization, Resources, Supervision.

## Data availability

Data will be made available on request.

## Declaration of Competing Interest

The authors declare that they have no known competing financial interests or personal relationships that could have appeared to influence the work reported in this paper.

## Acknowledgments

The authors would like to thank the Natural Science Foundation of Shandong Province of China (Nos. ZR2020MB024) and the Open Project Program of Guangdong Provincial Key Laboratory for Electronic Functional Materials and Devices, Huizhou University (No. EFMD2021001Z) for financially supporting this work.

## Appendix A. Supporting information

Supplementary data associated with this article can be found in the online version at doi:10.1016/j.jallcom.2023.169713.

## References

[1] S. Chang, H. Zhang, Z. Zhang, FeCo alloy/N, S dual-doped carbon composite as a high-performance bifunctional catalyst in an advanced rechargeable zinc-air battery, J. Energy Chem. 56 (2021) 64–71.
[2] C. Deng, K.-H. Wu, J. Scott, S. Zhu, R. Amal, D.-W. Wang, Ternary MnO/CoMn alloy@N-doped graphitic composites derived from a bi-metallic pigment as bifunctional electrocatalysts, J. Mater. Chem. A 7 (2019) 20649–20657.
[3] S. Li, C. Cheng, X. Zhao, J. Schmidt, A. Thomas, Active salt/silica-templated 2D mesoporous FeCo-$N_x$ -carbon as bifunctional oxygen electrodes for zinc-air batteries, Angew. Chem. Int. Ed. Engl. 57 (2018) 1856–1862.
[4] Z. Wang, J. Ang, J. Liu, X.Y.D. Ma, J. Kong, Y. Zhang, T. Yan, X. Lu, FeNi alloys encapsulated in N-doped CNTs-tangled porous carbon fibers as highly efficient and durable bifunctional oxygen electrocatalyst for rechargeable zinc-air battery, Appl. Catal. B 263 (2020) 118344–118355.
[5] J.-T. Ren, Y.-S. Wang, L. Chen, L.-J. Gao, W.-W. Tian, Z.-Y. Yuan, Binary FeNi phosphides dispersed on N,P-doped carbon nanosheets for highly efficient overall water splitting and rechargeable Zn-air batteries, Chem. Eng. J. 389 (2020) 124408–124459.
[6] M. Wang, H. Wang, J. Ren, X. Wang, R. Wang, FeCo nanoclusters inserted N,S –doped carbon foams as bifunctional electrocatalyst for high-performance rechargeable Zn-air batteries, J. Power Sources 538 (2022) 231592–231598.
[7] H. Xu, H. Jia, H. Li, J. Liu, X. Gao, J. Zhang, M. Liu, D. Sun, S. Chou, F. Fang, R. Wu, Dual carbon-hosted Co-$N_3$ enabling unusual reaction pathway for efficient oxygen reduction reactio, Appl. Catal. B 297 (2021) 120390–120398.
[8] H. Yang, X. Han, A.I. Douka, L. Huang, L. Gong, C. Xia, H.S. Park, B.Y. Xia, Advanced oxygen electrocatalysis in energy conversion and storage, Adv. Funct. Mater. 31 (2020).
[9] Z. Cao, H. Hu, M. Wu, K. Tang, T. Jiang, Planar all-solid-state rechargeable Zn–air batteries for compact wearable energy storage, J. Mater. Chem. A 7 (2019) 17581–17593.
[10] N. Xue, J. Liu, P. Wang, C. Wang, S. Li, H. Zhu, J. Yin, Scalable synthesis of $Fe_3N$ nanoparticles within N-doped carbon frameworks as efficient electrocatalysts for oxygen reduction reaction, J. Colloid Interface Sci. 580 (2020) 460–469.
[11] J. Ding, P. Wang, S. Ji, H. Wang, V. Linkov, R. Wang, N-doped mesoporous $FeN_x$/carbon as ORR and OER bifunctional electrocatalyst for rechargeable zinc-air batteries, Electrochim. Acta 296 (2019) 653–661.
[12] A.A. Eissa, S.G. Peera, N.H. Kim, J.H. Lee, g-$C_3N_4$ templated synthesis of the $Fe_3C$@NSC electrocatalyst enriched with Fe–$N_x$ active sites for efficient oxygen reduction reaction, J. Mater. Chem. A 7 (2019) 16920–16936.
[13] K. Tang et al., Hydrophobization Engineering of the Air-Cathode Catalyst for Improved Oxygen Diffusion towards Efficient Zinc-Air Batteries, Angew. Chem. Int. Ed. Engl. 61 (2022) e202202671- e202202678.
[14] J. Ding, S. Ji, H. Wang, V. Linkov, H. Gai, F. Liu, Q. Liu, R. Wang, N-doped 3D porous Ni/C bifunctional electrocatalysts for alkaline water electrolysis, ACS Sustain. Chem. Eng. 7 (2019) 3974–3981.
[15] Z.-q Cao, M.-z Wu, H.-b Hu, G.-j Liang, C.-y Zhi, Monodisperse $Co_9S_8$ nanoparticles in situ embedded within N, S-codoped honeycomb-structured porous carbon for bifunctional oxygen electrocatalyst in a rechargeable Zn–air battery, NPG Asia Mater. 10 (2018) 670–684.
[16] K. Tang, C. Yuan, Y. Xiong, H. Hu, M. Wu, Inverse-opal-structured hybrids of N, S-codoped-carbon-confined Co9S8 nanoparticles as bifunctional oxygen electrocatalyst for on-chip all-solid-state rechargeable Zn-air batteries, Appl. Catal. B 260 (2020) 118209–118220.
[17] D. Deng, L. Yu, X. Chen, G. Wang, L. Jin, X. Pan, J. Deng, G. Sun, Iron encapsulated within pod-like carbon nanotubes for oxygen reduction reaction, Angew. Chem. Int. Ed. Engl. 52 (2013) 371–375.
[18] J. Xiao, Y. Xu, Y. Xia, J. Xi, S. Wang, Ultra-small $Fe_2N$ nanocrystals embedded into mesoporous nitrogen-doped graphitic carbon spheres as a highly active, stable, and methanol-tolerant electrocatalyst for the oxygen reduction reaction, Nano Energy 24 (2016) 121–129.
[19] X. Huang, Z. Yang, B. Dong, Y. Wang, T. Tang, Y. Hou, In situ $Fe_2N$@N-doped porous carbon hybrids as superior catalysts for oxygen reduction reaction, Nanoscale 9 (2017) 8102–8106.
[20] T. Li, M. Li, M. Zhang, X. Li, K. Liu, M. Zhang, X. Liu, D. Sun, L. Xu, Y. Zhang, Y. Tang, Immobilization of $Fe_3N$ nanoparticles within N-doped carbon nanosheet frameworks as a high-efficiency electrocatalyst for oxygen reduction reaction in Zn-air batteries, Carbon 153 (2019) 364–371.
[21] X. Li, Y. Zhang, J. Zhang, C. Wang, Isolated Fe atoms dispersed on cellulose-derived nanocarbons as an efficient electrocatalyst for the oxygen reduction reaction, Nanoscale 11 (2019) 23110–23115.
[22] J.D. Rodney, S. Deepapriya, M. Cyril Robinson, C. Justin Raj, S. Perumal, B.C. Kim, S. Jerome Das, Lanthanum doped copper oxide nanoparticles enabled proficient bi-functional electrocatalyst for overall water splitting, Int. J. Hydrog. Energy 45 (2020) 24684–24696.
[23] H. Wang, A. Guan, J. Zhang, Y. Mi, S. Li, T. Yuan, C. Jing, L. Zhang, L. Zhang, G. Zheng, Copper-doped nickel oxyhydroxide for efficient electrocatalytic ethanol oxidation, Chin. J. Catal. 43 (2022) 1478–1484.
[24] T. Kwon, T. Kim, Y. Son, K. Lee, Dopants in the design of noble metal nanoparticle electrocatalysts and their effect on surface energy and coordination chemistry at the nanocrystal surface, Adv. Energy Mater. 11 (2021) 2100265–2100296.
[25] K. Siddharth, Y. Hong, X. Qin, H.J. Lee, Y.T. Chan, S. Zhu, G. Chen, S.-I. Choi, M. Shao, Surface engineering in improving activity of Pt nanocubes for ammonia electrooxidation reaction, Appl. Catal. B 269 (2020) 118821–118828.
[26] Y. Hong, C.H. Choi, S.I. Choi, Catalytic surface specificity of $Ni(OH)_2$ -decorated Pt nanocubes for the hydrogen evolution reaction in an alkaline electrolyte, ChemSusChem 12 (2019) 4021–4028.
[27] B.M. Hunter, H.B. Gray, A.M. Muller, Earth-abundant heterogeneous water oxidation catalysts, Chem. Rev. 116 (2016) 14120–14136.
[28] F.L.-U. Eduardo Cruz-Silva, Emilio Muñoz-Sandoval, Bobby G. Sumpter, Humberto Terrones, Jean-Christophe Charlier, Vincent Meunier, Mauricio Terrones, Electronic transport and mechanical properties of phosphorus- and phosphorus–nitrogen-doped carbon nanotubes, ACS Nano 3 (2009) 1913–1921.
[29] X.K. Kong, C.L. Chen, Q.W. Chen, Doped graphene for metal-free catalysis, Chem. Soc. Rev. 43 (2014) 2841–2857.
[30] S.S. Shinde, A. Sami, J.-H. Lee, Lanthanides-based graphene catalysts for high performance hydrogen evolution and oxygen reduction, Electrochim. Acta 214 (2016) 173–181.
[31] N. Liu, D. Cao, W. Liu, H. Zhang, Y. Zhu, L. Chang, D. Wu, D. Cheng, Constructing La-doped ultrathin Co-based nanostructured electrocatalysts for high-performance water oxidation process, Int. J. Hydrog. Energy 47 (2022) 14504–14514.
[32] W. Sun, C. Ma, X. Tian, J. Liao, J. Yang, C. Ge, W. Huang, An amorphous lanthanum–iridium solid solution with an open structure for efficient water splitting, J. Mater. Chem. A 8 (2020) 12518–12525.
[33] Z. Zhang, S. Liu, X. Li, T. Qin, L. Wang, X. Bo, Y. Liu, L. Xu, S. Wang, X. Sun, Y. Lu, F. Luo, S. Liu, Lewis-basic lanthanide metal-organic framework-derived versatile multi-active-site synergistic catalysts for oxygen reduction reaction, ACS Appl. Mater. Interfaces 10 (2018) 22023–22030.
[34] F. Zhang, S. Ji, H. Wang, H. Liang, X. Wang, R. Wang, Implanting cobalt atom clusters within nitrogen-doped carbon network as highly stable cathode for lithium-sulfur batteries, Small Methods 5 (2021) 2100066–2100076.
[35] J. Ding, S. Ji, H. Wang, B.G. Pollet, R. Wang, Mesoporous CoS/N-doped Carbon as HER and ORR bifunctional electrocatalyst for water electrolyzers and zinc-air batteries, ChemCatChem 11 (2019) 1026–1032.
[36] P. Yin, X. Luo, Y. Ma, S.-Q. Chu, S. Chen, X. Zheng, J. Lu, X.-J. Wu, H.-W. Liang, Sulfur stabilizing metal nanoclusters on carbon at high temperatures, Nat. Commun. 12 (2021) 3135–3144.
[37] Y.C. Wang, L.Y. Wan, P.X. Cui, L. Tong, Y.Q. Ke, T. Sheng, M. Zhang, S.H. Sun, H.W. Liang, Y.S. Wang, K. Zaghib, H. Wang, Z.Y. Zhou, J. Yuan, Porous carbon membrane-supported atomically dispersed pyrrole-type $FeN_4$ as active sites for electrochemical hydrazine oxidation reaction, Small 16 (2020) 2002203–2002210.
[38] Y.-C. Wang, L. Huang, P. Zhang, Y.-T. Qiu, T. Sheng, Z.-Y. Zhou, G. Wang, J.-G. Liu, M. Rauf, Z.-Q. Gu, W.-T. Wu, S.-G. Sun, et al., Constructing a triple-phase interface in micropores to boost performance of Fe/N/C catalysts for direct methanol fuel cells, ACS Energy Lett. 2 (2017) 645–650.
[39] Y. Pang, Z. Mo, H. Wang, X. Wang, V. Linkov, R. Wang, Manganese-assisted annealing produces abundant macropores in a carbon aerogel to enhance its oxygen reduction catalytic activity in zinc–air batteries, ACS Sustain. Chem. Eng. 9 (2021) 5526–5535.
[40] H. Wang, Y. Pang, Z. Mo, X. Wang, J. Ren, R. Wang, Performance evaluation of functionalized carbon aerogel as oxygen reduction reaction electrocatalyst in zinc-air cell, J. Power Sources 511 (2021) 230458–230466.
[41] J. Zhang, J. Lian, Q. Jiang, G. Wang, Boosting the OER/ORR/HER activity of Ru-doped Ni/Co oxides heterostructure, Chem. Eng. J. 439 (2022) 135634–135643.

[42] X. Zheng, X. Cao, Z. Sun, K. Zeng, J. Yan, P. Strasser, X. Chen, S. Sun, R. Yang, Indiscrete metal/metal-N-C synergic active sites for efficient and durable oxygen electrocatalysis toward advanced Zn-air batteries, Appl. Catal. B 272 (2020) 118967–118976.
[43] C. Xu, Z. Lin, D. Zhao, Y. Sun, Y. Zhong, J. Ning, C. Zheng, Z. Zhang, Y. Hu, Facile in situ fabrication of Co nanoparticles embedded in 3D N-enriched mesoporous carbon foam electrocatalyst with enhanced activity and stability toward oxygen reduction reaction, J. Mater. Sci. 54 (2019) 5412–5423.
[44] I.S. Amiinu, X. Liu, Z. Pu, W. Li, Q. Li, J. Zhang, H. Tang, H. Zhang, S. Mu, From 3D ZIF nanocrystals to Co-$N_x$/C nanorod array electrocatalysts for ORR, OER, and Zn-air batteries, Adv. Funct. Mater. 28 (2018) 1704638–1704646.
[45] X. Zhang, Z. Zhu, Y. Tan, K. Qin, F.X. Ma, J. Zhang, Co, Fe codoped holey carbon nanosheets as bifunctional oxygen electrocatalysts for rechargeable Zn-air batteries, Chem. Commun. 57 (2021) 2049–2052.
[46] Y. He, X. Yang, Y. Li, L. Liu, S. Guo, C. Shu, F. Liu, Y. Liu, Q. Tan, G. Wu, Atomically dispersed Fe–Co dual metal sites as bifunctional oxygen electrocatalysts for rechargeable and flexible Zn–air batteries, ACS Catal. 12 (2022) 1216–1227.
[47] Z. Zhao, M. Li, L. Zhang, L. Dai, Z. Xia, Design principles for heteroatom-doped carbon nanomaterials as highly efficient catalysts for fuel cells and metal-air batteries, Adv. Mater. 27 (2015) 6834–6840.
[48] L. Lai, J.R. Potts, D. Zhan, L. Wang, C.K. Poh, C. Tang, H. Gong, Z. Shen, J. Lin, R.S. Ruoff, Exploration of the active center structure of nitrogen-doped graphene-based catalysts for oxygen reduction reaction, Environ. Sci. Technol. 5 (2012) 7936–7942.
[49] C. Sun, S. Ji, H. Wang, X. Wang, R. Wang, Effect of surface reconstruction induced by different electrochemical methods on hydrogen evolution performance of $Ni_2P$ array catalysts, Int. J. Hydrog. Energy 47 (2022) 17097–17106.
[50] R. Wang, Q. Dong, H. Wang, S. Ji, X. Wang, V. Linkov, Molten-salt media synthesis of N-doped carbon tubes containing encapsulated Co nanoparticles as bifunctional air cathode for zinc-air batteries, Chem. Eur. J. 26 (2020) 10752–10758.